



# Fe/N/S-doped mesoporous carbon nanostructures as electrocatalysts for oxygen reduction reaction in acid medium



Da-Hee Kwak<sup>a</sup>, Sang-Beom Han<sup>a</sup>, Young-Woo Lee<sup>b</sup>, Hyun-Suk Park<sup>a</sup>, In-Ae Choi<sup>a</sup>, Kyeng-Bae Ma<sup>a</sup>, Min-Cheol Kim<sup>a</sup>, Si-Jin Kim<sup>a</sup>, Do-Hyoung Kim<sup>a</sup>, Jung-Inn Sohn<sup>b</sup>, Kyung-Won Park<sup>a,\*</sup>

<sup>a</sup> Department of Chemical Engineering, Soongsil University, Seoul, 156-743, Republic of Korea

<sup>b</sup> Department of Engineering Science, University of Oxford, Oxford, OX1 3PJ, United Kingdom

## ARTICLE INFO

### Article history:

Received 24 August 2016

Received in revised form 6 October 2016

Accepted 31 October 2016

Available online 1 November 2016

### Keywords:

Iron

Nitrogen

Sulfur

Mesoporous carbon

Oxygen reduction reaction

## ABSTRACT

Many alternatives to typical Pt-based catalysts have been developed to enhance oxygen reduction reaction (ORR) performance in acid medium due to their scarcity and high activation loss during the ORR. We synthesized mesoporous carbon nanostructures with multi-dopants such as iron, nitrogen, and sulfur as a cathode catalyst using the ordered silica templates and porphyrinic iron. The co-doped mesoporous carbon cathode catalysts exhibited a high ORR performance in an acid medium, i.e. complete ORR process and improved durability. The enhanced ORR properties of the catalysts might be ascribed to iron-containing catalytic active sites surrounded by nitrogen/sulfur species and a well-defined mesoporous carbon nanostructure.

© 2016 Elsevier B.V. All rights reserved.

## 1. Introduction

Polymer electrolyte membrane fuel cells (PEMFCs) are promising electrochemical power sources due to their high energy conversion efficiency, power density, low emission of pollutants, and low operating temperatures [1–5]. As electrocatalysts of PEMFCs, platinum (Pt) based nanoparticles supported on carbon are well known to be utilized as the most active oxygen reduction reaction (ORR) catalysts in cathodes. However, the expensive Pt-based catalysts in the PEMFCs have exhibited still high over-potentials of ORR, instability of the catalysts caused by agglomeration between catalyst nanoparticles during a long-term operation, and corrosion of carbon supports [3,6–8]. Therefore, a variety of promising candidates have been proposed to overcome this problem by developing non-precious metal (NPM) catalysts with high ORR activity such as nitrogen-doped carbon nanotube or graphene and transition metal complexes with porphyrin ligands [4,9–12]. Recent studies on pyrolyzed Fe nitrogen-doped and Fe/Co nitrogen-doped carbon catalysts for ORR have shown high activity and durability [5,13,14]. Since Jasinski and co-workers reported that transition metal-N<sub>4</sub>

chelate macrocycles could be used to enhance ORR activities [15], various macrocyclic transition-metal compounds have been investigated. The transition metal-N<sub>4</sub> compounds such as metal phthalocyanine (MPc) and metal porphyrins complex as an active sites have facilitated a complete process of four-electron transfer reaction in the ORR [6,16–29]. Recently, the iron-tetramethoxy-phenylporphyrin chloride (FeTMPPCl)-based catalysts with Fe-N<sub>4</sub> compounds have showed an improved electrocatalytic properties and selectivity [30–32]. To form N-containing NPM catalysts for ORR, MPc, which possesses a unique conjugated ligand including eight N atoms in a unit structure, and the central metal ion in the molecule, has been explored as the catalyst precursor. The pyrolyzed Co- and Fe-centered Pcs have been proved to be the most promising catalysts, which were reported to have a comparable ORR activity to that of commercial Pt/C catalyst [33–36]. In addition, the activity of the catalysts prepared by M-Pc precursors was affected by the kind of core metal as follows: Fe > Co > Ni > Cu [32,37–39].

The heteroatoms such as S [40–43], P [44,45], and B [46–49] doped graphitic structures exhibited an enhanced ORR activity, resulting from improved charge transfer, reduced overpotential, and induced oxygen adsorption [50]. Particularly, it has been reported that the synergistic effect between the N and S was found to be very strong, resulting in high performing ORR catalysts

\* Corresponding author.

E-mail address: [kwpark@ssu.ac.kr](mailto:kwpark@ssu.ac.kr) (K.-W. Park).

[51–55]. Qing et al. reported nitrogen-sulfur doped carbon (derived from pyrolyzing carbon-supported copper phthalocyanine tetrasulfonic acid tetrasodium salt) as a highly efficient metal-free catalyst for the ORR in alkaline medium [33]. Wang and co-workers suggested the N and S doped graphene catalysts using thiourea with a remarkable ORR performance in alkaline medium [52]. You et al. synthesized the doped graphene nanostructures as ORR catalysts using dipyrrole-methane, pyridine, thiophene, bithiophene as nitrogen and Sulfur sources [55]. Compared to Pt, although electrocatalysts based on carbon and/or graphene have exhibited superior ORR activities in alkaline medium, the ORR properties of the NPM catalysts in acid medium should be still improved through the formation of an optimized Fe-N coordination structure in the N-doped carbons [4,5,56–66].

In this study, co-doped mesoporous carbon nanostructures as a cathode catalyst were synthesized using ordered mesoporous silica (SBA-15) as templates with transition metalloporphyrin and sulfur precursors. The resulting carbon frameworks containing iron-incorporated pyridinic N and thiophenic S into the graphene sheets were fabricated [5]. The high surface area and mesoporous structure in the catalysts could be responsible for excellent ORR performance in alkaline and acid medium [50–71]. Furthermore, the high active site density and strong capability for charge- and mass-transport of the catalysts will be essential requirements to remarkably upgrade the catalytic performance. On the basis of the above considerations, we prepared co-doped well-defined mesoporous carbon nanostructures as a cathode catalyst using template method and co-doping process [71]. The co-doped mesoporous samples were characterized using field-emission transmission electron microscopy (FE-TEM), field emission scanning electron microscopy (FE-SEM), X-ray diffraction (XRD), X-ray photoelectron spectroscopy (XPS), and Raman spectrometry. The nitrogen adsorption/desorption isotherms of the samples were obtained to measure specific surface areas and pore size distributions of the samples. The ORR performance of the samples was evaluated and compared using electrochemical measurement in half and single cell [7].

## 2. Experimental

### 2.1. Synthesis of doped mesoporous carbon nanostructures

Silica template (SBA-15) was prepared using P123 triblock copolymer ( $\text{EO}_{20}\text{PO}_{70}\text{EO}_{20}$ ) (Fig. 1(a)). Pluronic P123 (SIGMA ALDRICH, 8.0 g) was completely dissolved in de-ionized (DI) water (60 g) and 2 M HCl solution (240 g) and tetraethyl orthosilicate (TEOS, SIGMA ALDRICH, 17 g) was then added in the solution. The mixture solution was stirred for 20 h at 35 °C and maintained at 80 °C for 24 h. The obtained products were washed and filtrated with DI water several times. After the complete washing, the products were dried in 50 °C oven for 12 h and heated at 600 °C for 4 h under an air atmosphere [72]. Synthesis of co-doped mesoporous carbon nanostructures was performed using a solid-state method that utilized a silica template and 5,10,15,20-tetrakis(4-methoxyphenyl)-21H,23H-porphyrin iron(III) chloride (FeTMPP, SIGMA ALDRICH) as iron, nitrogen, and carbon sources, and thioacetamide (TAA, SIGMA ALDRICH) as a sulfur source (Fig. 1(b)) [5,73,74]. The silica template was mixed with FeTMPP in the absence or presence of TAA. Furthermore, the samples were synthesized with different weight ratios of FeTMPP to TAA in the same way [75]. The obtained mixtures were placed in quartz boats and pyrolyzed at 900 °C for 3 h in an  $\text{N}_2$  atmosphere (Fig. 1(c)). To remove the silica template, the pyrolyzed samples was washed with 10 wt% hydrofluoric acid solution for 2 h, washed with DI

water and ethanol, and dried in a 50 °C oven for 12 h (Fig. 1(d)) [5].

### 2.2. Structural analysis

The morphology of the samples was visualized using FE-SEM (JEOL, JSM-6700F). The structure and chemical composition of the samples were characterized using FE-TEM (Philips Tecnai F20 system operating at 200 kV) and energy dispersive X-ray (EDX) spectroscopy. XRD analysis (Bruker D2 Phase system equipped with a  $\text{Cu K}_\alpha$  radiation source of  $\lambda = 0.15406 \text{ nm}$  and a Ni filter) was performed to confirm the crystal structure of the as-prepared samples. Raman spectra were obtained using a high resolution Raman spectrometer (Horiba Jobin Yvon, LabRAM HR UV/Vis/NIR photoluminescence). To analyse the surface area and pore structure, nitrogen adsorption and desorption isotherms were measured using a Micromeritics ASAP 2020 at 77 K. The chemical state and elemental composition were confirmed by XPS (Thermo Scientific, K-Alpha) with  $\text{Al K}_\alpha$  X-ray source of 1486.8 eV. Thermal gravimetric analysis (TGA, SDTA851, Mettler Toledo) was carried out to determine the mass ratio of the samples at a heating rate of  $5 \text{ }^\circ\text{C min}^{-1}$  under an air atmosphere [7,41].

### 2.3. Electrochemical analysis

The electrochemical characterization of the samples was performed in a typical electrochemical cell using a potentiostat (CH Instrument, CHI 700C). The graphitic rod and Ag/AgCl (saturated in 3 M KCl) were used as counter and reference electrodes, respectively [62]. All electrode potential was converted into RHE [4,5,62]. The ring-disk electrode (RRDE), which polished with 1, 0.3, and  $0.05 \mu\text{m}$   $\text{Al}_2\text{O}_3$  pastes and washed in DI water, was used as a working electrode. The catalyst ink was prepared by mixing the catalyst powder with DI water, isopropanol (IPA, SIGMA ALDRICH), and 5 wt% Nafion solution (SIGMA ALDRICH).  $1.0 \mu\text{L}$  catalyst ink ( $\sim 600 \mu\text{g}_{\text{catalyst}} \text{ cm}^{-2}$ ) was dropped on the rotating disk electrode with a surface area of  $0.126 \text{ cm}^2$  and dried in a 50 °C oven. For comparison, 20 wt% Pt/Vulcan XC-72 (Premetek Co.) with an average particle size of 3.5–4 nm ( $\sim 40 \mu\text{g}_{\text{catalyst}} \text{ cm}^{-2}$ ) was utilized. Cyclic voltammograms (CVs) and linear sweep voltammograms (LSVs) of the samples were obtained in 0.5 M  $\text{H}_2\text{SO}_4$  solution. The stability test was conducted in the range of 0.7 and 1.2 V in  $\text{O}_2$ -saturated 0.5 M  $\text{H}_2\text{SO}_4$  for 10,000 cycles with a scan rate of  $50 \text{ mV s}^{-1}$ . The role of iron and methanol-tolerance in the ORR process were evaluated using ORR polarization curves in  $\text{O}_2$ -saturated 0.5 M  $\text{H}_2\text{SO}_4$  with 10 mM KCN and  $\text{O}_2$ -saturated 0.5 M  $\text{H}_2\text{SO}_4$  with 1.0 M  $\text{CH}_3\text{OH}$ , respectively [7].

### 2.4. Fabrication of membrane electrode assembly and unit cell measurement

The membrane electrode assembly (MEA) was fabricated by decal method with Fe/N-MC(1:1) and Fe/N/S-MC(1:1:1) as cathode catalysts. The catalyst ink was prepared by mixing 0.2 g catalyst with DI water, IPA, and 5 wt% Nafion solution. The ink was coated on Teflon film using ultrasonic spraying and transferred into pre-treated solid-state Nafion membrane (211, DuPont) by hot-pressing at 120 °C under 100 atm for 2 min. The amount of the cathode catalyst with a content of 50 wt% Nafion was  $\sim 3.0 \text{ mg cm}^{-2}$ . The electrode deposited with Pt(20 wt%)/C on carbon paper ( $\sim 0.5 \text{ mg}_{\text{Pt}} \text{ cm}^{-2}$ ) was used as an anode. The MEA was fabricated with anode and membrane with cathode by hot-pressing at 120 °C under 100 atm for 2 min. The fabricated MEA was inserted between graphite plates with a serpentine flow-field (active area  $\sim 5 \text{ cm}^2$ ) and metal plates as current collectors and assembled for a single cell measurement. The PEMFC perfor-

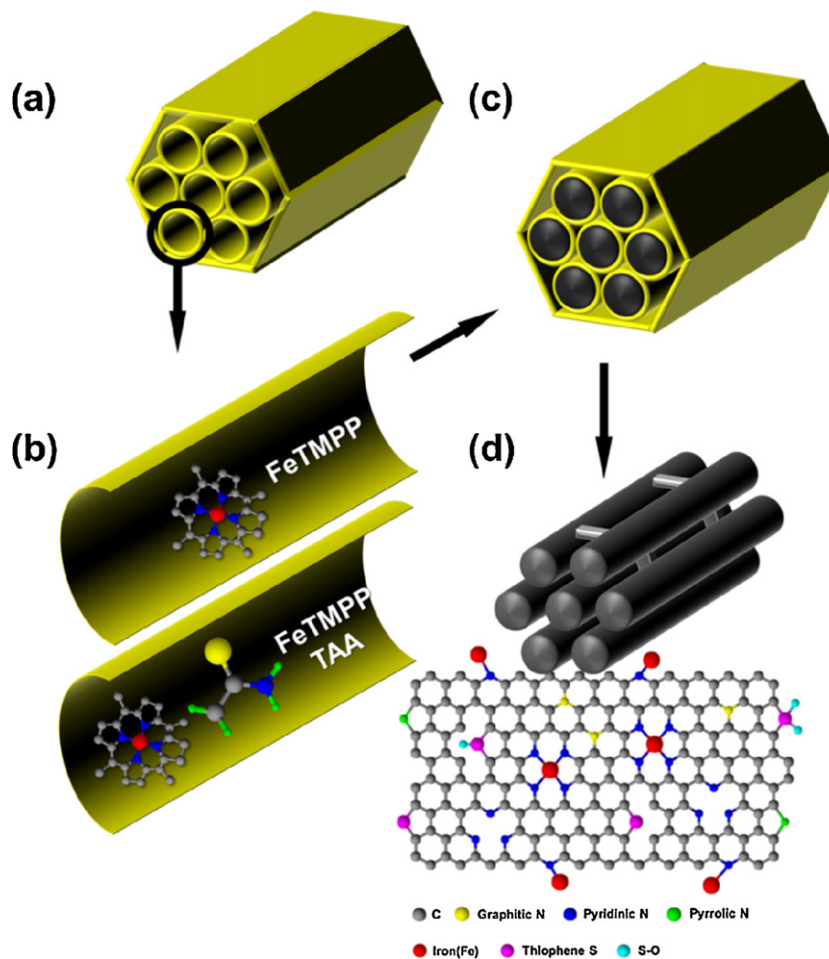


**Fig. 1.** Synthesis of sulfur and nitrogen co-doped mesoporous carbon nanostructures as an ORR catalyst in acid medium: (a) Preparation of the template, (b) adding dopants into the template, (c) pyrolysis of the mixture, and (d) removal of the template.

mance was evaluated at 80 °C under an ambient pressure using a computer-controlled electronic load (CNLPEM005-01, CNL Energy Co.). The hydrogen and oxygen gas humidified at 65 °C were supplied with flow rates of 100 and 300 mL min<sup>-1</sup>, respectively.

### 3. Results and discussion

The dopant content and species of the heteroatoms within the framework of doped carbon nanostructures (denoted as Fe/N-MC(X:Y) and Fe/N/S-MC(X:Y:Z), respectively), which could affect an electrocatalytic performance of the NPM catalysts, were manipulated using mass ratios of (template: FeTMPP) and (template: FeTMPP: TAA), respectively. To compare the ORR properties of the samples with different ratios of template: FeTMPP: TAA in an acid medium, the polarization curves were obtained in O<sub>2</sub>-saturated 0.5 M H<sub>2</sub>SO<sub>4</sub>, as shown in Fig. 2, compared to the commercial Pt/C catalyst (20 wt.% Pt on Vulcan XC-72, Premetek Co.). Among these NPM catalysts, Fe/N-MC(1:1) and Fe/N/S-MC(1:1:1), synthesized in the absence and presence of TAA, respectively, exhibited relatively excellent ORR properties; *i.e.* more positive onset potentials and more higher half-wave potentials. Especially, it is noticeable that Fe/N/S-MC(1:1:1) exhibits the most excellent ORR activity in an acid medium.

The silica template (denoted as m-SiO<sub>2</sub>) synthesized using pluronic P123 triblock copolymer for the doped mesoporous carbon nanostructures exhibits a tube-type mesoporous structure with a relatively uniform pore diameter of 4.1 nm, as observed

in FE-SEM and FE-TEM images (Figs. S1(a)-S1(c) in the Supporting information). The doped mesoporous carbon nanostructures were prepared using a template method by heating at 900 °C for 3 h under an N<sub>2</sub> atmosphere using m-SiO<sub>2</sub> template, followed by removing m-SiO<sub>2</sub> template. The morphologies of the Fe/N-MC(1:1) and Fe/N/S-MC(1:1:1) were examined using FE-SEM and FE-TEM. Figs. S1(d) and S1(e) show SEM images of the carbon nanostructures prepared using m-SiO<sub>2</sub>. The samples exhibited a rod shape similar to m-SiO<sub>2</sub> template with a uniform size implying the complete transfer of templates into the nanostructures [76]. The carbon nanostructures show a tube-type mesoporous structure with a pore size of ~4.9 nm, maintaining the frame structure of the template without any serious collapse. All of the nanostructures exhibited a cylindrical channel with a thin wall of ~4.2 nm thickness, representing the complete transfer of m-SiO<sub>2</sub> template into the carbon nanostructures accompanied by homogeneous coating on SiO<sub>2</sub> surfaces during the synthesis process. Furthermore, to identify the elemental distribution of the mesoporous carbon structures, as shown in Figs. S1(f) and S1(g), mapping images of carbon, nitrogen/sulfur, and iron were obtained using a high-angle annular dark-field scanning TEM-EDX spectroscopy. It is evident that the as-prepared samples contain carbon and dopants (iron, nitrogen, and sulfur) homogeneously distributed along the mesoporous nanostructures. In particular, despite the acid treatment during the synthesis, iron element was incorporated with carbon, nitrogen, and sulfur species in the nanostructures, demonstrating that the Fe-N in the doped carbon nanostructures can be electrochemical

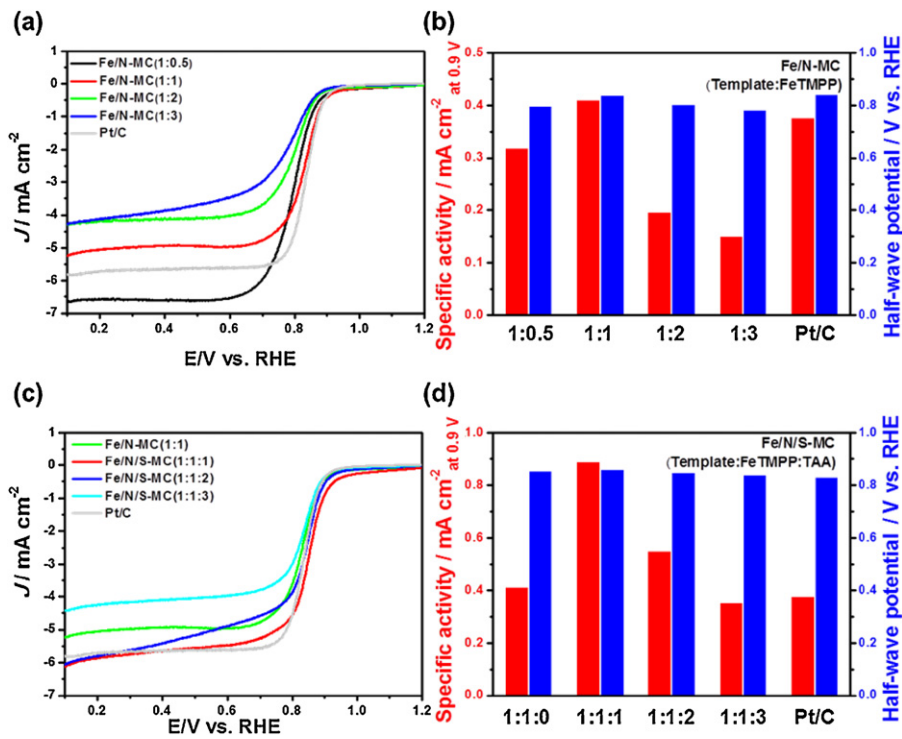


**Fig. 2.** LSVs ((a), (c)) and comparison ((b), (d)) of the samples as cathode catalysts in  $O_2$ -saturated 0.5 M  $H_2SO_4$  with a scan rate of 5 mV s<sup>-1</sup> and an electrode rotating speed of 1600 rpm at 25 °C.

active sites for the ORR. The excellent replication of Fe/N-MC(1:1) and Fe/N/S-MC(1:1:1) from m-SiO<sub>2</sub> as a template can be confirmed from the wide-angle XRD patterns. As shown in the wide-range XRD patterns (Fig. 3(a)), despite the broad XRD peak at ~11.4° due to the partial formation of graphene oxide, the main peaks for the (002) and (101) planes of the as-prepared samples suggest that the carbon nanostructures consist of a graphitic carbon framework [69,77,78]. As shown in Fig. 3(b), Raman spectra of Fe/N-MC(1:1) and Fe/N/S-MC(1:1:1) contained two characteristic peaks corresponding to G (1584 cm<sup>-1</sup>) and D band (1350 cm<sup>-1</sup>), which are indicative of a  $E_{2g}$  vibration mode in  $sp^2$  carbon structure and a disordered structure caused by doping effect, respectively [79,80]. The ratios of peak areas measured from D and G bands in the Fe/N-MC(1:1) and Fe/N/S-MC(1:1:1) are 3.51 and 3.72, respectively. The larger area ratios may be attributed to the structural defects caused by pyrolysis with FeTMPP and/or TAA as precursors, namely iron-nitrogen-sulfur doping [7]. To characterize the specific surface area of the as-prepared co-doped mesoporous carbon nanostructures, nitrogen gas adsorption-desorption isotherms were obtained, as shown in Fig. 3(c) and (d). The specific surface areas of Fe/N-MC(1:1) and Fe/N/S-MC(1:1:1) are ~983.7 and ~1064.6 m<sup>2</sup> g<sup>-1</sup>, respectively. Especially, the high specific surface area and mesopore of ~2.8 nm of the Fe/N/S-MC(1:1:1) are responsible for the enhanced ORR activity by facilitating mass transport and increasing electrochemical active sites [75,81–83]. The specific surface areas and pore sizes of Fe/N/S-MC(1:1:2) and Fe/N/S-MC(1:1:3) are ~796.7 and ~526.3 m<sup>2</sup> g<sup>-1</sup>, respectively, and ~2.9 and ~3.1 nm, respectively (Fig. 3(e) and (f)). With the increased TAA content, the specific surface areas of Fe/N/S-MC samples were gradually decreased due to the partial shrink of the carbon nanostructure caused by the increasing sulfur doping [76]. However, Fe/N/S-MC(1:1:1) with an optimized content of sulfur exhibited an improved specific surface area due to a synergistic effect by S and N as dopants compared to Fe/N-MC(1:1) [55,75,76].

XPS analysis was carried out to confirm the chemical contents and states of the elements in the as-prepared nanostructures. The

XPS survey spectra for Fe/N-MC(1:1) and Fe/N/S-MC(1:1:1) displayed the dominant presence of C and N on the nanostructure surfaces (Fig. 4(a)) [75]. As shown in Fig. 4(b) and (c), the carbon phases in the Fe/N-MC(1:1) and Fe/N/S-MC(1:1:1) consisted of C–C (284.6 eV), C–N (285.6 eV), C–O (286.2 eV), and O=C–O (288.5 eV). Also, Fe/N-MC(1:1) and Fe/N/S-MC(1:1:1) exhibited nitrogen contents of ~4.26 and ~4.57 at.%, respectively, with various nitrogen species (Fig. 4(d) and (e)). The fine-scan N 1s spectra of the samples consisted of pyridinic (398.3 ~ 399.5 eV), pyrrolic (400.1 ~ 400.9 eV), graphitic (401.2 ~ 402.0 eV), and oxidized nitrogen (403.4 ~ 410.0 eV) [84]. The nitrogen functional groups incorporated in the carbon structures could be usually found in the following chemical states [79–87]: (1) Pyridinic N combined with 2 carbon atoms and located at edge or defect in the graphene plane could provide one p-electron per a hexagonal aromatic p-system. (2) Pyrrolic N combined with two carbon atoms and located at edge or defect site in the graphene plate has two p-electrons per a p-system. (3) Graphitic (or quaternary) N could be exchanged with carbon atom in the graphene plane and located in the graphene layer [5,28,88–93]. Fe/N-MC(1:1) and Fe/N/S-MC(1:1:1) exhibited these characteristic peaks formed by pyrolysis of FeTMPP, which could be expected to be an effective ORR active site [11,85]. However, the question of which one of the nitrogen functional groups in the carbon nanostructures might be a dominant ORR active site is still controversial [94]. It was reported that pyridinic or pyrrolic N might increase the density of electronic state, demonstrating N-doping effect, and could be an electrocatalytic active site for ORR [13,85,95,96]. On the other hand, a recent study suggested that graphitic N was more important for an electrocatalytic activity of the nitrogen-doped carbons [55]. The carbon atoms, which are positioned as neighbours of nitrogen dopants, have a considerably high positive charge density and strong electronic affinity, resulting in an improved oxygen adsorption and ORR activity [95–97]. As shown in Fig. 4(f), Fe/N-MC(1:1) contained much higher content of the pyrrolic N than Fe/N/S-MC(1:1:1), while the portion of the pyridinic N state in Fe/N/S-MC(1:1:1) increased compared to

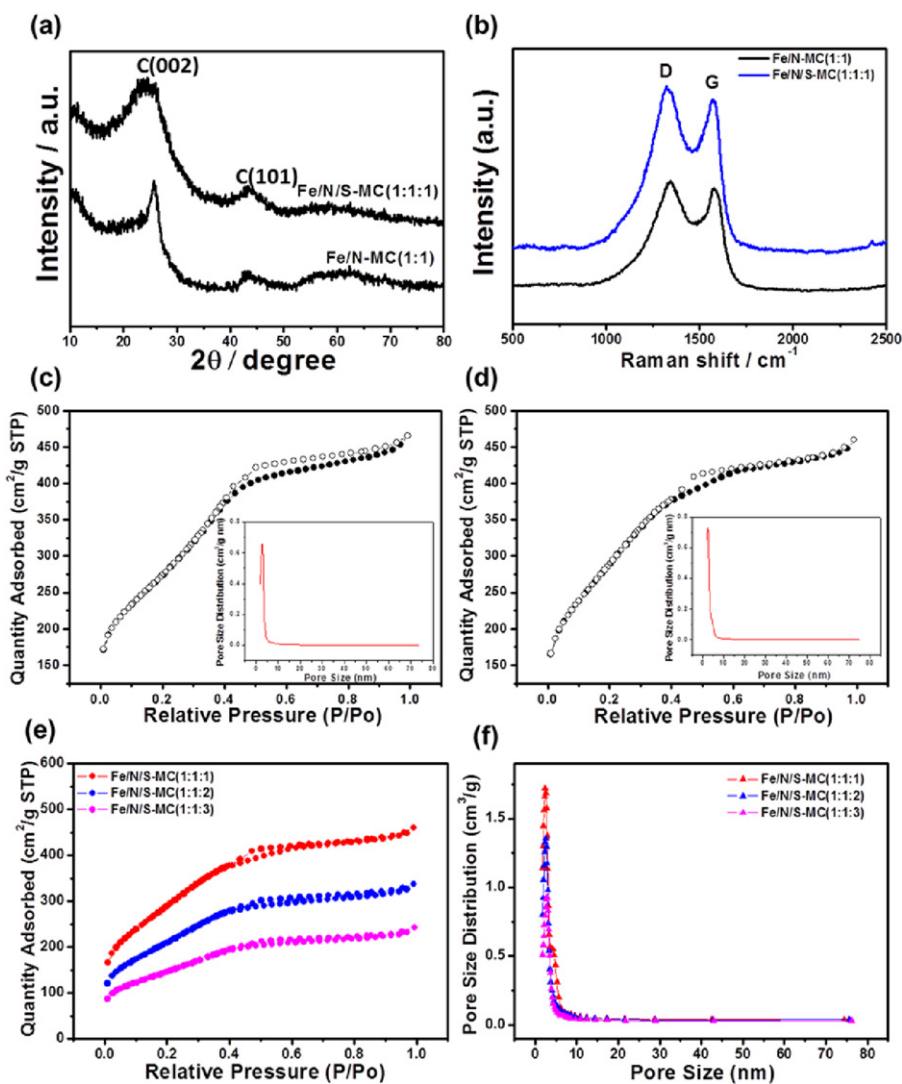


**Fig. 3.** (a) Wide-range XRD patterns and (b) Raman spectra of Fe/N-MC(1:1) and Fe/N/S-MC(1:1:1). Nitrogen adsorption-desorption isotherms and pore size distributions (insets) of (c) Fe/N-MC(1:1) and (d) Fe/N/S-MC(1:1:1). (e) Nitrogen adsorption-desorption isotherms and (f) pore size distributions of the Fe/N/S-MC samples.

Fe/N-MC(1:1). It has been reported that the higher content of the pyrrolic N or pyridinic N states might be attributed to metal doping into N-doped carbon nanostructures, resulting in the bonding formation between metal and nitrogen, *i.e.* metal–N<sub>4</sub> or metal–N<sub>3</sub> macrocycles [11,13,85]. It was reported that since increased pyridinic N sites in N-doped carbon materials could be favourable for ORR, as a result, the metal doping in the doped carbon nanostructures could be correlated with the contents of pyrrolic N or pyridinic N bonding [98–100]. The Fe2p XPS spectra of the samples contained Fe2p<sub>3/2</sub> and Fe2p<sub>1/2</sub> at 710.9 and 721 eV, respectively (Fig. 4(g) and (h)). Actually, the Fe/N/S-MC(1:1:1) exhibited a higher iron content of ~0.48 at.%, in comparison with Fe/N-MC(1:1) (~0.42 at.%), dominantly forming the Fe-pyridinic N (Fig. 4(f)) as a main active site for the ORR. TGA curves of the Fe/N-MC(1:1) and Fe/N/S-MC(1:1:1) were obtained in the range of 20–900 °C at a heating rate of 5 °C min<sup>−1</sup> under an air flow of 60 cm<sup>3</sup> min<sup>−1</sup> (Fig. S2). The residual amounts in the Fe/N-MC(1:1) and Fe/N/S-MC(1:1:1) were ~3.5 and ~5.8 wt.%, respectively, as a result of an oxidation of iron as a residual material. The actual iron amounts in the Fe/N-MC(1:1) and Fe/N/S-MC(1:1:1) were determined to be ~2.4 and ~4.1 wt.%, respectively. The high resolution S2p peak of Fe/N/S-MC(1:1:1) can be resolved into three different peaks at the binding energies of 163.9, 165.1, and 167.8 eV, respectively (Fig. 4(i)). The

thiophene–S contained 2p<sub>3/2</sub> (–C–S–C–) and 2p<sub>1/2</sub> (–C=S–) at 163.9 and 165.1 eV, respectively, as a spin-orbit coupling and 3rd peak at 167.8 eV corresponding to oxidized sulfur [29,40,75,101,102]. The –C–S–C– species have been identified previously as an active site for the increasing ORR activity [33]. The relative mass ratio of FeTMPP to TAA is an experimental condition to elaborate manipulate the dopant content and species of the nitrogen and sulfur within carbon framework of final products. When the mass ratios of FeTMPP to TAA with the fixed ratio of template to FeTMPP(1:1) are 1:1, 1:2, and 1:3, the nitrogen contents of Fe/N/S-MC(1:1:1), Fe/N/S-MC(1:1:2), and Fe/N/S-MC(1:1:3) are 4.57, 2.81, and 3.02 at.%, respectively (Fig. S3). It was found that after doping with S, the portion of pyridinic N state increased. Moreover, the co-doping of N and S could provide a surrounding chemical environment, which makes pyridinic N species more preferable. Consequently, the electrochemical performance is expected to be potentially enhanced due to the synergistic effect of N and S in Fe/N/S-MC [103].

To analyse typical electrochemical properties for the samples, the CVs were obtained in Ar-saturated 0.5 M H<sub>2</sub>SO<sub>4</sub> with a scan rate of 50 mV s<sup>−1</sup> (Fig. S4(a)). No significant oxidation-reduction peaks in the as-prepared samples were observed within the given potential range. Thus, the carbon samples exhibited the double-layer capacitance which depends on specific surface area, porous

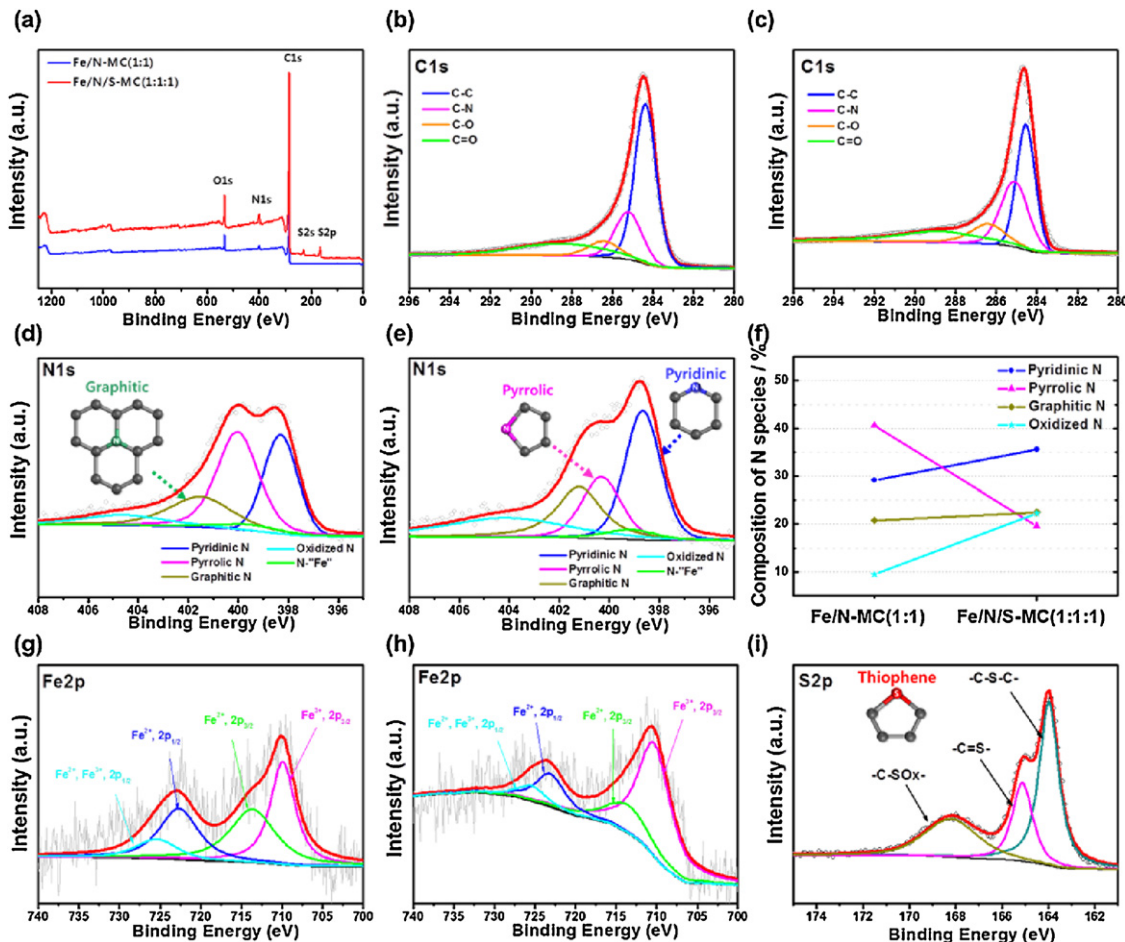


**Fig. 4.** (a) XPS survey spectra of Fe/N-MC(1:1) and Fe/N/S-MC(1:1:1). C1 s XPS spectra of (b) Fe/N-MC(1:1) and (c) Fe/N/S-MC(1:1:1). N1 s XPS spectra of (d) Fe/N-MC(1:1) and (e) Fe/N/S-MC(1:1:1). (f) Comparison of N species of the as-prepared doped mesoporous carbon nanostructures. Fe2p XPS spectra of (g) Fe/N-MC(1:1) and (h) Fe/N/S-MC(1:1:1). (i) S2p XPS spectrum of Fe/N/S-MC(1:1:1).

structure, and surface functional states [95–97]. As shown in Fig. S4(b), the specific capacitances of Fe/N/S-MC(1:1:1) ( $\sim 393.5 \text{ F g}^{-1}$ ) and Fe/N-MC(1:1) ( $\sim 218.6 \text{ F g}^{-1}$ ) are higher than Vulcan XC-72R ( $\sim 119.1 \text{ F g}^{-1}$ ) [104–111]. In particular, the remarkably improved capacitance of Fe/N/S-MC(1:1:1) can be attributed to a high active surface area, large accessible well-defined pore structure, and surface functional states, facilitating then accessibility of oxygen molecule as an oxidant [110,111]. Fig. 5 shows CVs of the as-prepared samples obtained in Ar- and O<sub>2</sub>-saturated 0.5 M H<sub>2</sub>SO<sub>4</sub> to evaluate their ORR properties in an acid medium. The Fe/N-MC(1:1) and Fe/N/S-MC(1:1:1) exhibited oxygen reduction peak potentials at 0.78 and 0.80 V, respectively (Fig. 5(a) and (b)), demonstrating an improved ORR activity of the Fe/N/S-MC(1:1:1) with the more positive peak potential compared to Fe/N-MC(1:1). The polarization curves of the samples were measured using a rotating ring disk electrode (RRDE) in O<sub>2</sub>-saturated 0.5 M H<sub>2</sub>SO<sub>4</sub> (Fig. 5(c) and (d)). The Fe/N/S-MC(1:1:1) showed a more positive on-set potential of  $\sim 0.94 \text{ V}$  and an improved half-wave potential ( $E_{1/2}$ ) of  $\sim 0.86 \text{ V}$  Fe/N-MC(1:1) compared to the Fe/N-MC(1:1), implying a superior ORR activity of Fe/N/S-MC(1:1:1) to Fe/N/S-MC(1:1) (Fig. 5(c)). From the RRDE polarization curves, as shown in Fig. 5(d), an electron-transfer number ( $n$ ) and hydrogen peroxide (%H<sub>2</sub>O<sub>2</sub>) of the samples during the ORR were determined by the following equations:

$$n = 4 \times \frac{I_D}{\left(\frac{I_R}{N}\right) + I_D}$$

$$H_2O_2 (\%) = 200 \times \frac{\frac{I_R}{N}}{\left(\frac{I_R}{N}\right) + I_D}$$

where  $I_D$ ,  $I_R$ , and  $N$  are the current on the carbon electrode, the current on the Pt ring-disk electrode, the collecting coefficient number of  $-0.4245$  in this case, respectively [7]. The Fe/N/S-MC(1:1:1) showed an electron-transfer number of  $\sim 4$ , and low%H<sub>2</sub>O<sub>2</sub> yield toward ORR at all potential range, in comparison with Fe/N-MC(1:1), demonstrating a complete electron transfer during the ORR and remarkable ORR activity. Obviously, sulfur species such as  $-\text{C}-\text{S}-\text{C}-$  can be as an active site for the increasing ORR activity even similar to nitrogen. Thus, it can be concluded that the enhanced ORR activity of the Fe/N/S-MC(1:1:1) could be attributed to the doped N and S species serving as the ORR electrocatalytic sites [33].

The stability test of the samples was conducted by cycling between 0.4 and 0.9 V with a scan rate of  $50 \text{ mV s}^{-1}$  in O<sub>2</sub>-saturated 0.5 M H<sub>2</sub>SO<sub>4</sub>. After the 10,000 cycling stability test, Fe/N/S-MC(1:1:1) exhibited a relatively slight negative shift of  $\sim 27 \text{ mV}$  in the half-wave potential compared to Fe/N/S-MC(1:1) ( $\sim 48 \text{ mV}$ ) and Pt/C ( $\sim 63 \text{ mV}$ ) (Figs. 6(a)–(c)). In direct methanol fuel cells (DMFCs), the cathode catalysts for the ORR need to be tolerant of CH<sub>3</sub>OH as a fuel, which could transport through the membrane from the anode, showing no methanol electrooxidation current at the cathode. As shown in Figs. 6(d)–6(f), the ORR polarization curves of the samples were compared in the absence and

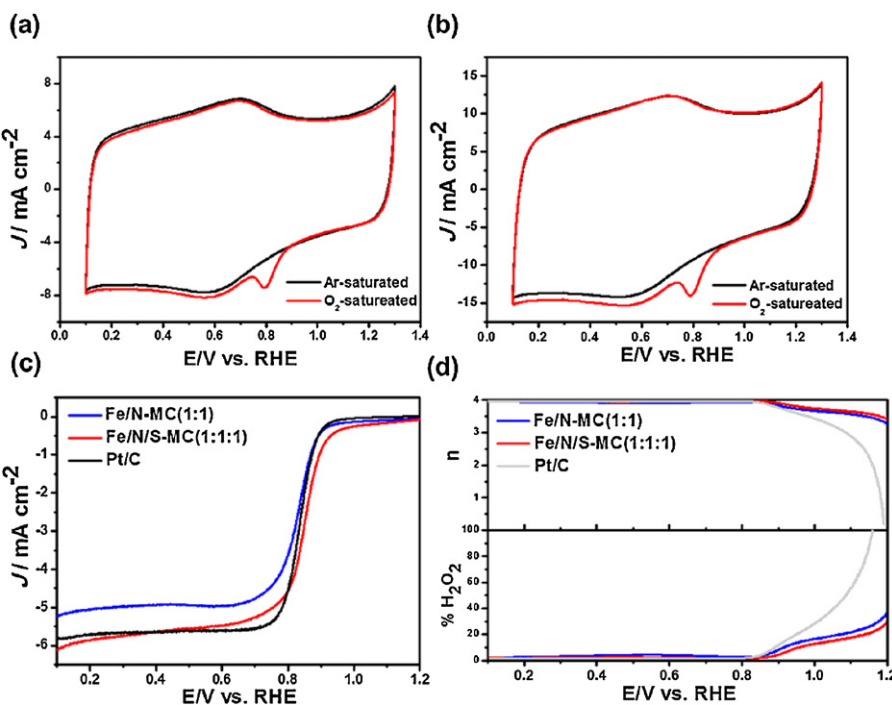


**Fig. 5.** CVs of (a) Fe/N-MC(1:1) and (b) Fe/N/S-MC(1:1:1) in Ar- or  $\text{O}_2$ -saturated 0.5 M  $\text{H}_2\text{SO}_4$  with a scan rate of  $50 \text{ mV s}^{-1}$  at  $25^\circ\text{C}$ . (c) LSVs of the samples in  $\text{O}_2$ -saturated 0.5 M  $\text{H}_2\text{SO}_4$  with a scan rate of  $5 \text{ mV s}^{-1}$  and an electrode rotating speed of 1600 rpm at  $25^\circ\text{C}$ . (d) Plots of the electron-transfer number ( $n$ ) and generation yield of hydrogen peroxide ( $\% \text{H}_2\text{O}_2$ ) during the ORR.

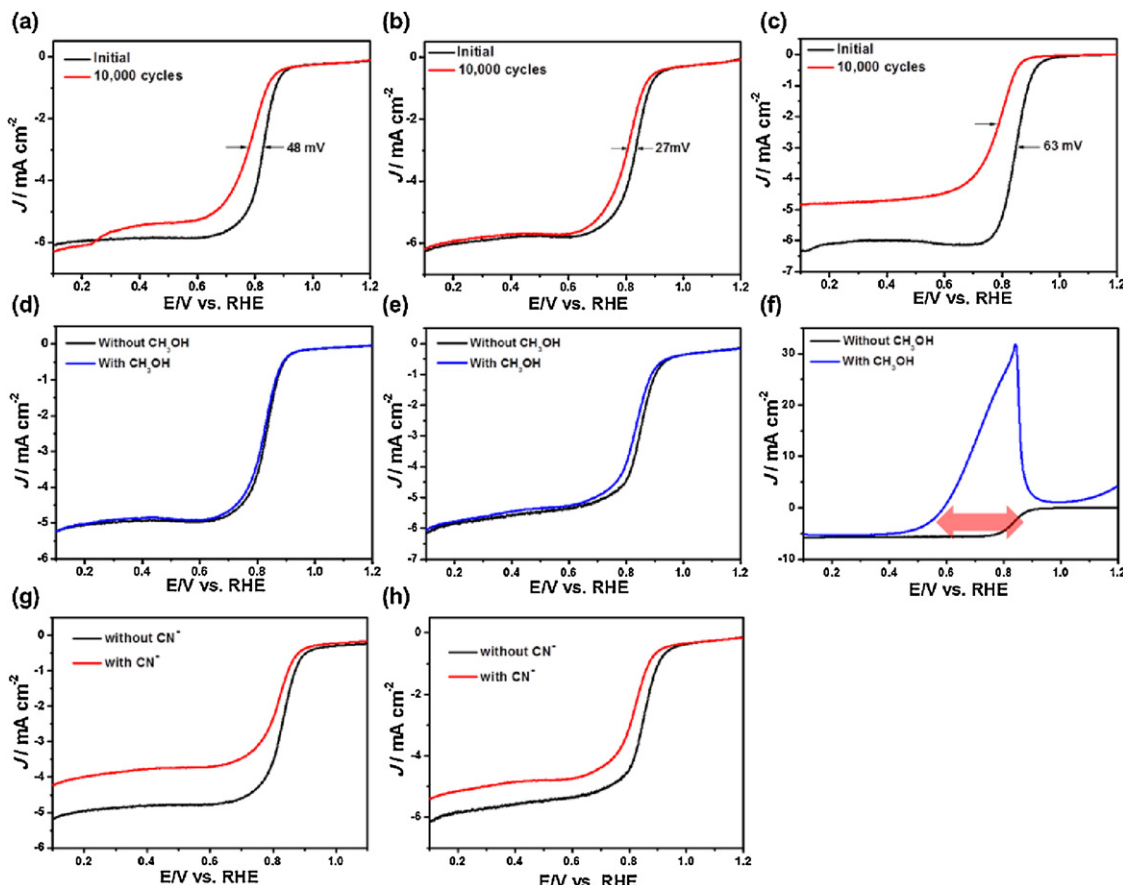


**Fig. 6.** LSVs of (a) Fe/N-MC(1:1), (b) Fe/N/S-MC(1:1:1), and (c) Pt/C with a scan rate of  $5 \text{ mV s}^{-1}$  before and after the stability test in  $\text{O}_2$ -saturated 0.5 M  $\text{H}_2\text{SO}_4$ . The stability test was performed by applying between 0.7 and 1.2 V for 10,000 cycles with a scan rate of  $50 \text{ mV s}^{-1}$  in  $\text{O}_2$ -saturated 0.5 M  $\text{H}_2\text{SO}_4$  at  $25^\circ\text{C}$ . LSVs of (d) Fe/N-MC(1:1), (e) Fe/N/S-MC(1:1:1), and (f) Pt/C with a scan rate of  $5 \text{ mV s}^{-1}$  and 1600 rpm in  $\text{O}_2$ -saturated 0.1 M  $\text{H}_2\text{SO}_4$  w/and w/o 0.1 M  $\text{CH}_3\text{OH}$  at  $25^\circ\text{C}$ . LSVs of (g) Fe/N-MC(1:1) and (h) Fe/N/S-MC(1:1:1) with a scan rate of  $5 \text{ mV s}^{-1}$  and 1600 rpm in  $\text{O}_2$ -saturated 0.1 M  $\text{H}_2\text{SO}_4$  w/and w/o 10 mM  $\text{KCN}$ .

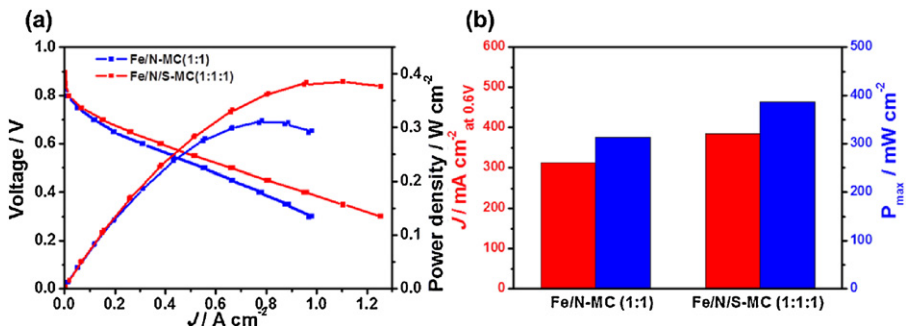


**Fig. 7.** (a) Polarization curves of the H<sub>2</sub>/O<sub>2</sub> PEMFCs with Fe/N-MC(1:1) and Fe/N/S-MC(1:1:1) as cathode catalysts at 80 °C. (b) Comparison of ORR performance for the NPM cathode catalysts.

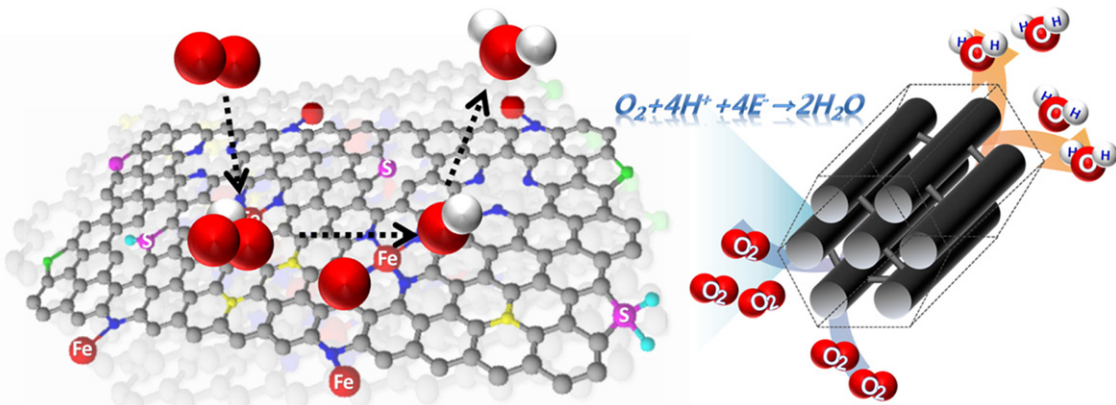


**Fig. 8.** D.-H. Kwak et al.

presence of CH<sub>3</sub>OH. Fe/N/S-MC(1:1:1) and Fe/N-MC(1:1) exhibited almost no loss of the ORR activity w/and w/o methanol demonstrating the methanol-tolerance of the doped carbon nanostructure catalysts. On the other hand, Pt/C showed a serious activity loss in the presence of methanol due to the electrocatalytic nature of Pt for methanol electrooxidation reaction even at the cathodic potentials.

Since the pyrrolic N or pyridinic N states might result in Fe-N<sub>4</sub> or Fe-N<sub>3</sub> macrocycles and improve the ORR catalytic activity, the role of iron as active catalytic sites for ORR was investigated in co-doped mesoporous carbon nanostructures as an electrocatalyst by comparing the ORR activity in O<sub>2</sub>-saturated 0.5 M H<sub>2</sub>SO<sub>4</sub> w/and w/o 10 mM KCN (Fig. 6(g) and (h)). Fe/N-MC(1:1) and Fe/N/S-MC(1:1:1) exhibited a deteriorated ORR activity in the presence of KCN. It has been reported that the CN<sup>-</sup> ions could be strongly combined with iron species [111]. In the present study, iron species as active sites in the doped carbon nanostructures might be combined with CN<sup>-</sup> ions in the O<sub>2</sub>-saturated solution, thus reducing active sites for the ORR and decreasing the ORR activity [7,112]. This suggests that both the iron and nitrogen species in the co-doped mesoporous carbon nanostructures are crucial active sites for ORR catalytic activity. Interestingly, Fe/N-MC(1:1) and Fe/N/S-MC(1:1:1) with the higher pyrrolic N and pyridinic N exhibited much lower ORR activity in the presence of 10 mM KCN.

Fig. 7(a) shows polarization curves of the PEMFCs measured at 80 °C under ambient pressure using Fe/N-MC(1:1) and Fe/N/S-MC(1:1:1) as cathode catalysts. Fe/N-MC(1:1) exhibited a maximal power density of ~313 mW cm<sup>-2</sup> and current density of ~312 mA cm<sup>-2</sup> at 0.6 V (Fig. 7(b)). On the other hand, Fe/N/S-MC(1:1:1) showed much enhanced performance: i.e. a maximal power density of ~386 mW cm<sup>-2</sup> and current density of ~385 mA cm<sup>-2</sup> at 0.6 V, compared to Fe/N-MC(1:1) (Fig. 7(b)). As

compared to the previous results of the PEMFCs using the NPM cathode catalysts (Table S1), an improvement in the performance using the Fe/N/S-MC(1:1:1) can be expected through an optimized MEA structure with an increased catalyst loading and high back pressure at the cathode in the PEMFCs [113]. The improved performance of the PEMFC using Fe/N/S-MC(1:1:1) as a cathode catalyst can be ascribed to the Fe/N-containing catalytic sites surrounded by nitrogen species, co-doping by sulfur, and a mesoporous nanostructure (Fig. 8) [53,71,113]. As summarized in Table S2, Fe/N/S-MC(1:1:1) having a fairly large specific surface area and an optimal ratio of dopants (Fe, N, and S) can be utilized as an ORR catalyst in an acid medium. However, the NPM cathode catalysts in the present study showed still lower ORR activity due to deteriorated mass transport caused by a thicker catalyst layer of ~140 μm, compared to a commercial Pt catalyst with ~40 μm (Fig. S5) [113,114]. Therefore, in order to further improve ORR performance of the doped mesoporous carbon nanostructures as a cathode catalyst in the single cell application, a further modification of the porous doped nanostructures and the MEA structure for the carbon-based NPM catalysts should be carried out as future works.

#### 4. Conclusions

In summary, we synthesized iron/nitrogen/sulfur-doped mesoporous carbon nanostructures as an ORR catalyst with iron coordinated by pyridinic N and thiophenic sulfur atoms. In particular, Fe/N/S-MC(1:1:1) exhibited high ORR current density, improved electron-transfer number, and excellent stability in an acid medium, even compared to Pt/C. The maximal power density of PEMFC using Fe/N/S-MC(1:1:1) can reach as high as ~386 mW cm<sup>-2</sup>. The improved ORR performance of the Fe/N/S-

MC(1:1:1) might be attributed to the electrocatalytic sites of nitrogen species combined with co-doping effect by sulfur, relatively large specific surface area, and well-defined mesoporous carbon nanostructure.

## Acknowledgments

This research was supported by Basic Science Research Program through the National Research Foundation of Korea (NRF) funded by the Ministry of Education (NRF-2016R1A2B2016033).

## Appendix A. Supplementary data

Supplementary data associated with this article can be found, in the online version, at <http://dx.doi.org/10.1016/j.apcatb.2016.10.084>.

## References

- [1] W. Liang, J. Chen, Y. Liu, S. Chen, *ACS Catal.* 4 (2014) 4170–4177.
- [2] H.A. Gasteiger, N. Markovic, *Science* 324 (2009) 48–49.
- [3] N.R. Sahraie, J.P. Paraknowitsch, C. Göbel, A. Thomas, P. Strasser, *J. Am. Chem. Soc.* 136 (2014) 14486–14497.
- [4] G. Wu, *Science* 334 (2011) 443–447.
- [5] J.Y. Cheon, T. Kim, Y. Choi, H.Y.M.G. Kim, Y.J. Sa, J. Kim, Z. Lee, T.-H. Yong, K. Kwon, O. Terasaki, G.-P. Park, R.R. Adzic, S.H. Joo, *Sci. Rep.* 3 (2013) 2715–2722.
- [6] H. Peng, Z. Mo, S. Liao, H. Liang, L. Yang, F. Luo, H. Song, Y. Zhong, B. Zhang, *Sci. Rep.* 3 (2013) 1765–1772.
- [7] J.-S. Moon, Y.-W. Lee, S.-B. Han, D.-H. Kwak, K.-H. Lee, A.-R. Park, J.I. Sohn, S.N. Cha, K.-W. Park, *Phys. Chem. Chem. Phys.* 16 (2014) 14644–14650.
- [8] Y. Yu, H. Li, H. Wang, X.-Z. Yuan, G. Wang, M. Pan, *J. Power Sources* 205 (2012) 10–23.
- [9] B. Wang, *J. Power Sources* 152 (2005) 1–15.
- [10] Y. Tang, B.L. Allen, D.R. Kauffman, A. Star, *J. Am. Chem. Soc.* 131 (2009) 13200–13201.
- [11] Y. Zhu, B. Zhang, X. Liu, D.-W. Wang, D.S. Su, *Angew. Chem. Int. Ed.* 53 (2014) 10673–10677.
- [12] H.-x. Zhong, J. Wang, Y.-w. Zhang, W.-l. Xu, W. Xing, D. Xu, Y.-f. Zhang, X.-b. Zhang, *Angew. Chem. Int. Ed.* 53 (2014) 14235–14239.
- [13] H. Yin, C. Zhang, F. Liu, Y. Hou, *Adv. Funct. Mater.* 24 (2014) 2930–2937.
- [14] M. Vikkisk, I. Kruusenberg, U. Joost, E. Shulga, I. Kink, K. Tammeveski, *Appl. Catal. B Environ.* 147 (2014) 369–376.
- [15] R. Jasinski, *Nature* 201 (1964) 1212–1213.
- [16] D.S. Su, G. Sun, *Angew. Chem. Int. Ed.* 50 (2011) 11570–11572.
- [17] C.V. Rao, Y. Ishikawa, *J. Phys. Chem. C* 116 (2012) 4340–4346.
- [18] D. Yu, E. Nagelli, F. Du, L. Dai, *J. Phys. Chem. Lett.* 1 (2010) 2165–2173.
- [19] S. Yuan, J. Shui, L. Grabstanowicz, C. Chen, S. Commet, B. Reprogli, T. Xu, L. Yu, D.-J. Liu, *Angew. Chem. Int. Ed.* 52 (2013) 8349–8353.
- [20] Y. Jiang, Y. Lu, X. Lv, D. Han, Q. Zhang, L. Niu, W. Chen, *ACS Catal.* 3 (2013) 1263–1271.
- [21] J.H. Zagal, F. Bedioui, J.-P. Dodelet, *N<sub>4</sub>-Macrocyclic Metal Complexes*, Springer, New York, 2006.
- [22] N. Ramaswamy, U. Tylus, Q. Jia, S. Mukerjee, *J. Am. Chem. Soc.* 135 (2013) 15443–15449.
- [23] J. Sun, Y.-H. Fang, Z.-P. Liu, *Phys. Chem. Chem. Phys.* 16 (2014) 13733–13740.
- [24] H. Schulenburg, S. Stankov, V. Schünemann, J. Radnik, I. Dorandt, S. Fiechter, P. Bogdanoff, H. Tributsch, *J. Phys. Chem. B* 107 (2003) 9034–9041.
- [25] S. Baranton, C. Coutanceau, C. Roux, F. Hahn, J.-M. Léger, *J. Electroanal. Chem.* 577 (2005) 223–234.
- [26] R. Baker, D.P. Wilkinson, J. Zhang, *Electrochim. Acta* 53 (2008) 6906–6919.
- [27] E. Yeager, *J. Mol. Catal.* 38 (1986) 5–25.
- [28] J.P. Collman, P. Denisovich, Y. Konai, M. Marrocco, M. Koval, F.C. Anson, *J. Am. Chem. Soc.* 102 (1980) 6027–6036.
- [29] T. Wu, H. Shen, L. Sun, L. Cheng, B. Liu, J. Shen, *New J. Chem.* 36 (2012) 1385–1391.
- [30] I. Herrmann, U.I. Kramm, J. Radnik, S. Fiechter, P. Bogdanoff, *J. Electrochem. Soc.* 156 (2009) B1283–B1292.
- [31] H. Fei, R. Ye, G. Ye, Y. Gong, Z. Peng, Z. Fan, E.L.G. Samuel, P.M. Ajayan, J.M. Tour, *ACS Nano* 8 (2014) 10837–10843.
- [32] U.I. Koslowski, I. Abs-Wurmbach, S. Fiechter, P. Bogdanoff, *J. Phys. Chem. C* 112 (2008) 15356–15366.
- [33] X. Qing, X. Shi, X. Ma, X. Fan, X. Bai, Z. Chen, Z. Qiao, J. Zhang, *J. Power Sources* 266 (2014) 88–98.
- [34] I. Kruusenberg, L. Matisen, K. Tammeveski, *J. Nanosci. Nanotechnol.* 13 (2013) 621–627.
- [35] I. Kruusenberg, L. Matisen, Q. Shah, A.M. Kannan, K. Tammeveski, *Int. J. Hydrogen Energy* 37 (2012) 4406–4412.
- [36] F. Meng, H. Zhong, D. Bao, J. Yan, Xinbo Zhang, *J. Am. Chem. Soc.* 138 (2016) 10226–10231.
- [37] L. Ding, Q. Xin, X. Zhou, J. Qiao, H. Li, H. Wang, *J. Appl. Electrochem.* 43 (2013) 43–51.
- [38] G. Faubert, G. Lalande, R. Côté, R. Guay, J.P. Dodelet, L.T. Weng, P. Bertrand, G. Dénès, *Electrochim. Acta* 41 (1996) 1689–1701.
- [39] Z.P. Li, B.H. Liu, *Appl. Electrochem.* 40 (2010) 475–483.
- [40] S. Yang, L. Zhi, K. Tang, X. Feng, X. Maier, K. Müllen, *Adv. Funct. Mater.* 22 (2012) 3634–3640.
- [41] J. Xu, Y. Zhao, C. Shen, L. Guan, *ACS Appl. Mater. Interfaces* 5 (2013) 2594–2601.
- [42] Z.-L. Wang, X.-F. Hao, Z. Jiang, X.-P. Sun, D. Xu, J. Wang, H.-X. Zhong, F.-L. Meng, X.-B. Zhang, *J. Am. Chem. Soc.* 137 (2015) 15070–15073.
- [43] Z.-L. Wang, D. Xu, J.-J. Xu, X.-B. Zhang, *Chem. Soc. Rev.* 43 (2014) 7746–7786.
- [44] Z.-W. Liu, F. Peng, H.-J. Wang, H. Yu, W.-X. Zheng, J. Yang, *Angew. Chem.* 123 (2011) 3315–3319.
- [45] C. Zhang, N. Mahmood, H. Yin, F. Liu, Y. Hou, *Adv. Mater.* 25 (2013) 4932–4937.
- [46] Y. Zheug, Y. Jiao, L. Ge, M. Jaroniec, S.Z. Qiao, *Angew. Chem. Int. Ed.* 52 (2013) 3110–3116.
- [47] S. Wang, L. Zhang, Z. Xia, A. Roy, D.W. Chang, D.W. Baek, L. Dai, *Angew. Chem. Int. Ed.* 51 (2012) 4209–4212.
- [48] M. Cattelan, S. Agnoli, M. Favaro, D. Garoli, F. Romanato, M. Meneghetti, A. Barinov, P. Dardin, G. Granozzi, *Chem. Mater.* 25 (2013) 1490–1495.
- [49] Y. Gong, H. Fei, X. Zou, S. Zhou, S. Yang, G. Ye, Z. Liu, Z. Peng, J. Lou, R. Vajtai, B.I. Yakobson, J.M. Tour, *Chem. Mater.* 27 (2015) 1181–1186.
- [50] S. Wang, E. Iyyamperumal, E. Roy, Y. Xue, D. Yu, L. Dai, *Angew. Chem. Int. Ed.* 50 (2011) 11756–11760.
- [51] K. Gong, K. Du, K. Xia, K. Durstock, L. Dai, *Science* 323 (2009) 760–764.
- [52] X. Wang, J. Wang, J. Wang, S. Dou, Z. Ma, J. Wu, J. Tao, A. Shen, C. Ouyang, Q. Liu, Q. Wang, *Chem. Commun.* 50 (2014) 4839–4842.
- [53] Y. Su, Y. Zhang, X. Zhuang, S. Li, D. Wu, D. Zhang, X. Feng, *Carbon* 62 (2013) 296–301.
- [54] Y. Chang, F. Hong, C. He, Q. Zhan, J. Liu, *Adv. Mater.* 25 (2014) 4794–4799.
- [55] J.-M. You, M.S. Ahmed, H.S. Han, J.E. Choe, Z. Üstündag, S. Jeon, *J. Power Sources* 275 (2015) 73–79.
- [56] S. Gupta, D. Tryk, I. Bae, W. Aldred, E. Yeager, *J. Appl. Electrochem.* 19 (1989) 19–27.
- [57] M. Lefèvre, J.P. Dodelet, *J. Phys. Chem. B* 106 (2002) 8705–8713.
- [58] F. Jaouen, M. Lefèvre, J.-P. Dodelet, M. Cai, *J. Phys. Chem. B* 110 (2006) 5553–5558.
- [59] M. Lefèvre, E. Proietti, F. Jaouen, J.-P. Dodelet, *Science* 324 (2009) 71–74.
- [60] F. Jaouen, V. Goellner, M. Lefèvre, J. Herranz, E. Proietti, J.P. Dodelet, *Electrochim. Acta* 87 (2013) 619–628.
- [61] Y. Li, W. Zhou, H. Wang, L. Xie, Y. Liang, F. Wei, J.-C. Idrobo, S.J. Pennycook, H. Dai, *Nat. Nanotechnol.* 7 (2012) 394–400.
- [62] H.T. Chung, J.H. Won, P. Zelenay, *Nat. Commun.* 4 (2013) 1922–1926.
- [63] Y. Li, Y. Gong, Y. Liang, J. Feng, J.-E. Kim, H. Wang, G. Hong, G. Zhang, H. Dai, *Nat. Commun.* 4 (2013) 1805–1811.
- [64] S. Zhang, H. Zhang, Q. Liu, S. Chen, J. Mater. Chem. A 1 (2013) 3302–3308.
- [65] C.-W. Tsai, M.-H. Tu, C.-J. Chen, T.-F. Hung, R.-S. Liu, W.-R. Liu, M.-Y. Lo, Y.-M. Peng, L. Zhang, J. Zhang, D.-S. Shy, X.-K. Xing, *RSC Adv.* 1 (2011) 1349–1357.
- [66] L. Wang, L. Zhang, J. Zhang, *Electrochim. Commun.* 13 (2011) 447–449.
- [67] M.-Q. Wang, W.-H. Yang, H.-H. Wang, C. Chen, Z.-Y. Zhou, S.-G. Sun, *ACS Catal.* 4 (2014) 3928–3936.
- [68] H.-W. Liang, W. Wei, Z.-S. Wu, Z. Feng, K. Müllen, *J. Am. Chem. Soc.* 135 (2013) 16002–16005.
- [69] H.-P. Cong, P. Wang, M. Gong, S.-H. Yu, *Nano energy* 3 (2014) 55–63.
- [70] J. Liang, Y. Jiao, M. Jaroniec, S.Z. Qiao, *Angew. Chem. Int. Ed.* 51 (2012) 11496–11500.
- [71] A. Kong, X. Zhu, Z. Han, Y. Yu, Y. Zhang, B. Dong, Y. Shan, *ACS Catal.* 4 (2014) 1793–1800.
- [72] S.-J. Kim, Y.-W. Lee, S.-B. Han, S.-B. Kim, W.-S. Kim, K.-W. Park, *Int. J. Electrochem. Sci.* 8 (2013) 3825–3833.
- [73] K.T. Lee, X. Ji, M. Rault, L.F. Nazar, *Angew. Chem. Int. Ed.* 48 (2009) 5661–5665.
- [74] Y. Jo, J.Y. Cheon, J. Yu, H.Y. Jeong, C.-H. Han, Y. Jun, S.H. Joo, *Chem. Commun.* 48 (2012) 8057–8059.
- [75] Z. Liu, H. Nie, Z. Yang, J. Zhang, Z. Jin, Y. Lu, Z. Xiao, S. Huang, *Nanoscale* 8 (2013) 3283–3288.
- [76] D. Zhang, Y. Hao, L. Zheng, Y. Ma, H. Feng, H. Luo, *J. Mater. Chem. A* 1 (2013) 7584–7591.
- [77] B. Qiu, Y. Deng, M. Du, M. Xing, J. Zhang, *Ultradispersed cobalt ferrite nanoparticles assembled in graphene aerogel for continuous photo-Fenton reaction and enhanced lithium storage performance*, *Sci. Rep.* 6 (2016) 29099–29109.
- [78] H. Dong, C. Liu, H. Ye, L. Hu, B. Fugetsu, W. Dai, Y. Cao, X. Qi, H. Lu, X. Zhang, *Three-dimensional nitrogen-doped graphene supported molybdenum disulfide nanoparticles as an advanced catalyst for hydrogen evolution reaction*, *Sci. Rep.* 5 (2015) 17542–17553.
- [79] H. Liu, Y. Zhang, R. Li, X. Sun, S. Désilets, H. Abou-Rachid, M. Jaidann, L.-S. Lussier, *Carbon* 48 (2010) 1498–1507.
- [80] D. Geng, S. Yang, Y. Zhang, J. Yang, J. Liu, R. Li, T.-K. Sham, X. Sun, S. Ye, S. Knights, *Appl. Surf. Sci.* 257 (2011) 9193–9198.
- [81] Y.-L. Liu, X.-Y. Xu, P.-C. Sun, T.-H. Chen, *Int. J. Hydrogen Energy* 40 (2015) 4531–4539.
- [82] G. Tao, L. Zhang, L. Chen, X. Cui, Z. Hua, M. Wang, J. Wang, Y. Chen, J. Shi, *Carbon* 86 (2015) 108–117.

[83] F.-L. Meng, Z.-L. Wang, H.-X. Zhong, J. Wang, J.-M. Yan, X.-B. Zhang, *Adv. Mater.* 28 (2016) 7948–7955.

[84] J. Yan, H. Meng, F. Xie, X. Yuan, W. Yu, W. Lin, W. Ouyang, D. Yuan, *J. Power Sources* 245 (2014) 772–778.

[85] K. Artyushkova, B. Kiefer, B. Halevi, A. Knop-Gericke, R. Schlogl, P. Atanassov, *Chem. Commun.* 49 (2013) 2539–2541.

[86] P.H. Matter, L. Zhang, U.S. Ozkan, *J. Catal.* 239 (2006) 83–96.

[87] R. Arrigo, M. Hävecker, R. Schlögl, D.S. Su, *Chem. Commun.* (2008) 4891–4893.

[88] L. Wang, S. Dou, J. Xu, H.K. Liu, S. Wang, J. Ma, S.X. Dou, *Chem. Commun.* 51 (2015) 11791–11794.

[89] L. Lai, J.R. Potts, D. Zhan, L. Wang, C.K. Poh, C. Tang, Z. Gong, Z. Shen, J. Lin, R.S. Ruoff, *Energy Environ. Sci.* 5 (2012) 7936–7942.

[90] M. Liu, R. Zhang, W. Chen, *Chem. Rev.* 114 (2014) 5117–5160.

[91] A. Morozan, B. Jousselme, S. Palacin, *Energy Environ. Sci.* 4 (2011) 1238–1254.

[92] C.W.B. Bezerra, L. Zhang, K. Lee, H. Liu, A.L.B. Marques, E.P. Margques, H. Wang, J. Zhang, *Electrochim. Acta* 53 (2008) 4937–4951.

[93] C. Zhang, U. Hao, H. Liao, Y. Hou, *Nano Energy* 2 (2013) 88–97.

[94] Y. Shao, J. Sui, G. Yin, Y. Gao, *Appl. Catal. B Environ.* 79 (2008) 89–99.

[95] S. Maldonado, K.J. Stevenson, *J. Phys. Chem. B* 109 (2005) 4707–4716.

[96] Y. Shao, S. Zhang, M.H. Engelhard, G. Li, G. Shao, Y. Wang, J. Liu, I.A. Aksay, Y. Lin, *J. Mater. Chem.* 20 (2010) 7491–7496.

[97] D. Geng, Y. Chen, Y. Chen, Y. Li, R. Li, X. Sun, S. Ye, S. Knights, *Energy Environ. Sci.* 4 (2011) 760–764.

[98] F. Buckel, F. Effenberger, C. Yan, A. Gölzhäuser, M. Grunze, *Adv. Mater.* 12 (2000) 901–905.

[99] N.P. Subramanian, X. Li, V. Nallathambi, S.P. Kumaraguru, H. Colon-Meracado, G. Wu, J.-W. Lee, B.N. Popov, *J. Power Sources* 188 (2009) 38–44.

[100] H. Kim, K. Lee, S.I. Woo, Y. Jung, *Phys. Chem. Chem. Phys.* 13 (2011) 17505–17510.

[101] C.H. Choi, M.W. Chung, S.H. Park, S.I. Woo, *Phys. Chem. Chem. Phys.* 15 (2013) 1802–1805.

[102] J.Y. Kim, P.J. Reucroft, M. Taghie, *Energy Fuels* 8 (1994) 886–889.

[103] Q. Shi, F. Peng, S. Liao, H. Wang, H. Yu, Z. Liu, B. Zhang, D. Su, *J. Mater. Chem. A* 1 (2013) 14853–14857.

[104] H. Shi, *Electrochim. Acta* 41 (1996) 1633–1639.

[105] D. Lozano-Castelló, D. Cazorla-Amorós, A. Linares-Solano, S. Shiraishi, H. Kurihara, A. Oya, *Carbon* 41 (2003) 1765–1775.

[106] G. Gryglewicz, J. Machnikowski, E. Lorenc-Grabowska, G. Lota, E. Frackowiak, *Electrochim. Acta* 50 (2005) 1197–1206.

[107] E. Frackowiaka, F. Béguin, *Carbon* 39 (2001) 937–950.

[108] G. Hasegawa, T. Deguchi, K. Kanamori, K. Kobayashi, H. Kageyama, T. Abe, K. Nakanishi, *Chem. Mater.* 27 (2015) 4703–4712.

[109] X. Zhai, J. Liu, P. Li, M. Zhong, C. Ma, H. Wang, Q. Guo, Y. Song, L. Zhi, *Int. J. Electrochem. Sci.* 7 (2012), 7403–7312.

[110] E. Frackowiaka, F. Béguin, *Carbon* 40 (2002) 1775–1787.

[111] J. Masa, W. Xia, M. Muhler, W. Schuhmann, *Angew. Chem. Int. Ed.* 54 (2015) 10102–10120.

[112] M.S. Thorum, J.M. Hankett, A.A. Gewirth, *J. Phys. Chem. Lett.* 2 (2011) 295–298.

[113] Y.-C. Wang, Y.-J. Lai, L. Song, Z.-Y. Zhou, J.-G. Liu, Q. Wang, X.-D. Yang, C. Chen, W. Shi, Y.-P. Zheng, M. Rauf, S.-G. Sun, *Angew. Chem. Int. Ed.* 54 (2015) 9907–9910.

[114] S. Lee, M. Choun, Y. Ye, J. Lee, Y. Mun, E. Kang, J. Hwang, Y.-H. Lee, C.-H. Shin, S.-H. Moon, S.-K. Kim, E. Lee, J. Lee, *Angew. Chem. Int. Ed.* 54 (2015) 9230–9234.